JAAS

PAPER

View Article Online
View Journal | View Issue



Cite this: *J. Anal. At. Spectrom.*, 2026, **41**, 1025

# Monitoring of the iron and oxygen impurities in liquid sodium by laser-induced breakdown spectroscopy with a gas protection component

Jingya Dong, *[ab] Ce Feng,[a] Lingwei Zeng, [c] Linyuan Cao,[a] Rongdong Wang,[a] Qingfu Zhu[a] and Hanliang Bo*[b]

Received 10th November 2025
Accepted 19th January 2026

DOI: 10.1039/d5ja00438a

rsc.li/jaas

Sodium is a preferred coolant in Generation IV nuclear reactors due to its excellent heat transfer and nuclear properties. However, decreased cooling efficiency, material corrosion and blockages can be caused by excessive amounts of impurities in the sodium. Conventional detection methods are unable to realize rapid, *in situ*, sensitive and accurate online sodium impurity monitoring owing to factors such as equipment size, service life and detection time. In this study, a laser-induced breakdown spectroscopy device with a gas protection component was proposed. This design not only prevents sodium aerosols or liquid sodium splashing from contaminating the optical lens, but also enables sensitive analysis of Fe and O in sodium, with limits of detection of 0.68 μg $g^{-1}$ and 0.11 μg $g^{-1}$ and RSDs of 7% and 4%, respectively. The results demonstrated that this method has potential application prospects in the nuclear industry and could provide a guarantee for the safe operation of sodium-cooled fast reactors.



## 1 Introduction

Sodium-cooled fast reactors have been considered a popular research topic for next-generation nuclear reactors due to their remarkable potential to enhance the sustainability of nuclear power generation. This reactor type demonstrates unique advantages by optimizing key indicators such as economy, environmental impact and safety. The fast-neuron spectrum in sodium-cooled fast reactors not only enables efficient conversion of long-lived actinides, thereby alleviating nuclear waste disposal problems but also significantly improves the utilization rate of uranium resources by efficiently converting fertile materials into fissionable fuels (conversion factors > 1).[1] In terms of operating parameters, the sodium-cooled fast reactor utilizes a first circuit output temperature of about 500 °C, which provides superior thermal efficiency performance compared to conventional pressurized water reactors or boiling water reactors.[2] With these advantages, sodium-cooled fast reactors occupy an important position in Generation IV nuclear energy systems.

Liquid sodium is ideal as a fast reactor coolant due to its excellent thermophysical properties, including a low neutron absorption cross-section, weak moderating ability, high thermal conductivity and a moderate coefficient of thermal expansion. However, there are significant technical challenges posed by the reactive chemistry of sodium, including corrosion and deposit clogging. Corrosion behavior is mainly influenced by the concentration of O impurities. The corrosion rate of the core shell and structural material and induced material embrittlement are accelerated by higher O concentration, which leads to degradation of the mechanical properties, even possibly leading to clogging of the coolant flow paths or failure of critical components.[3–5] In addition, deposits could be formed by excessive Fe impurities in the sodium, which impede coolant flow. Additionally, dissolved alloying elements may migrate in the circuit and undergo neutron activation, increasing the risk of radioactive contamination.[6,7] It is worth noting that fission products detected in the coolant are often a sign of a possible breakage of a fuel element.

In fast reactors, the detection methods of O and Fe impurities in liquid sodium are mainly electrochemical methods,[8] vacuum distillation[9] and vacuum distillation-atomic absorption spectroscopy.[7] These methods are mature and have potential for field application.[8] However, the electrochemical method still suffers from several critical limitations, such as a narrow applicable temperature range, insufficient selectivity, limited sensor lifetime and potential measurement interference. Vacuum distillation separates and enriches impurities to improve the limit of detection (LOD). Chun Xie summarized that this method has a minimum detection amount of 10 μg of O impurities with a relative standard deviation (RSD) of 9.0% when the O concentration in sodium is 10–100 μg $g^{-1}$.[10] Nevertheless, the contamination may be caused by the high-

[a]*Department of Reactor Engineering Technology, China Institute of Atomic Energy, Beijing, 102413, China. E-mail: dongjingya@cnncmail.cn*

[b]*Institute of Nuclear and New Energy Technology, Tsinghua University, Beijing, 100084, China. E-mail: bohl@tsinghua.edu.cn*

[c]*Research Centre of Analytical Instrumentation, School of Mechanical Engineering, Sichuan University, Chengdu, 610065, China*

temperature distillation, and a long time is needed for sample processing, making it difficult to realize continuous online monitoring. Vacuum distillation-atomic absorption spectroscopy is mainly used for the detection of iron impurities. This method can accurately determine specific metal impurities, but the equipment is complex, and it can be applied to only some elements. Moreover, vacuum distillation-atomic absorption spectroscopy cannot be used for real-time monitoring. Therefore, the development of an easy maintenance, low-cost, fast and *in situ* monitoring device for Fe and O impurities in high-temperature liquid sodium is essential for the safe and efficient operation of a sodium-cooled fast reactor.

Laser-induced breakdown spectroscopy (LIBS) has been widely used in the past two decades because of its excellent applicability and environmental adaptability.[11,12] It has demonstrated unique advantages in the field of nuclear energy.[13,14] As a rapid multi-element analysis tool, LIBS has been successfully applied in various disciplines such as medical diagnosis, precision agriculture and geological exploration.[15–17] The core principle of LIBS is to use high-energy laser pulses focused on the sample surface to form a transient plasma on a trace sample through inverse bremsstrahlung and multi-photon ionization effects. Characteristic radiation, allowing the observation of continuum spectra, ion spectral lines, atomic spectral lines and molecular bands, is released during plasma cooling. These optical signals are collected and analyzed by high-resolution spectrometers and intensified charge-coupled devices (ICCDs). In the nuclear industry, LIBS has successfully realized the detection of lead, indium and other metal impurities in liquid sodium, with a detection limit of 5 ppm.[18] Hence, LIBS technology combines broad-spectrum analytical capability, elemental specificity, and *in situ* detection, making it ideal for real-time monitoring of the composition of nuclear reactor materials, especially in critical scenarios such as liquid metal coolant impurity monitoring.

In this work, a LIBS device with a gas protection component (GP-LIBS) was proposed. The GP component is effective in preventing contamination of the optical lens caused by sodium aerosols generated by high-temperature liquid sodium or by splashing of liquid sodium due to laser kinetic energy acting on the liquid sodium. Moreover, the sensitive detection and quantitative analysis of Fe and O impurities in high-temperature liquid sodium coolant were realized. The device provides a new monitoring strategy and equipment for the impurity elements in the sodium coolant in sodium-cooled fast reactors, which has potential application in the nuclear industry and provides a guarantee for the safe operation of nuclear power plants.

## 2 Experimental

### 2.1 Instrument

Fig. 1(a) shows a schematic diagram of the system of GP-LIBS (Chengdu Aliben Technology Co., Ltd, China). The laser beam was emitted from an Nd:YAG laser (Chengdu Junmin Jiachuang Technology Co., Ltd, China) with a wavelength of 1064 nm and a laser energy of 100 mJ, and entered the sample chamber through the focus lens with a focal length of 160 mm and a flange viewing window made of JGS1. The sample chamber is composed of a flange viewing window, a copper seal, a GP component and a sample detection area, which are all made of 316L. The laser beam acted on the surface of the liquid sodium through the GP component after entering the sample chamber, generating a laser-induced plasma and emitting characteristic spectral lines. The emitted light was received by a fiber optic collimator on the side axis through the GP structure and the flange viewing window, and is transmitted to the ARYELLE200 echelle spectrometer (LTB Lasertechnik Berlin, Germany) with a resolution of 22∼93 pm through an optical fiber for splitting and output to a computer. At the bottom of the sample chamber, a heating device consisting of a ceramic heater, a thermocouple, a temperature controller, and heat preservation cotton was installed. The sodium was continuously heated to ensure that the sodium sample was always in the liquid state. To prevent the burning of high-temperature liquid sodium, a gas inlet and two gas outlets were left on the side of the sample

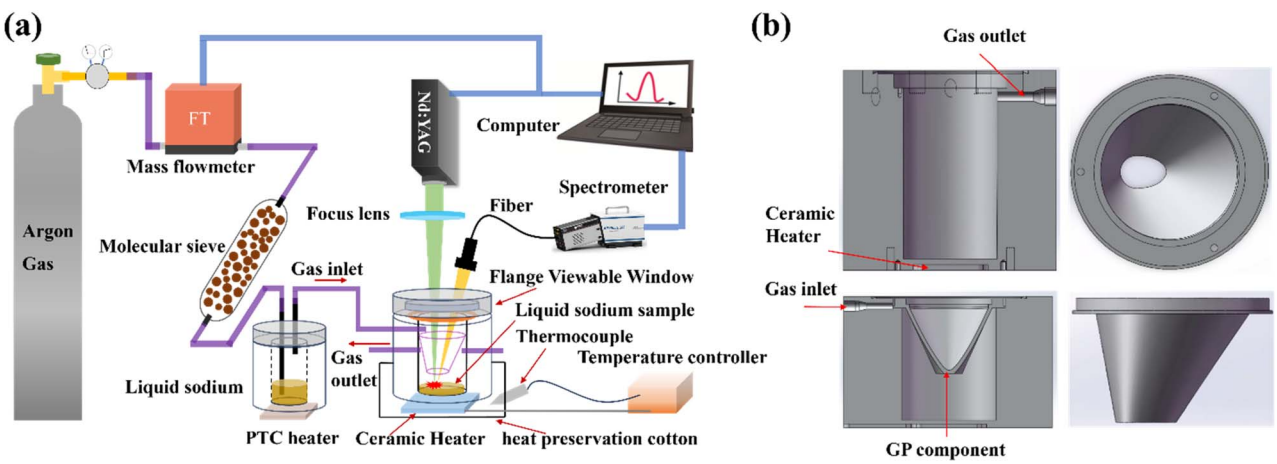


Fig. 1 A schematic diagram of the system of the GP-LIBS and the structure of the GP component. (a) A schematic diagram of the system of the GP-LIBS. (b) A schematic diagram of the sample chamber and the structure of the GP component.

 

chamber for the introduction of argon gas (purity of 99.999%) controlled by the mass flowmeter. Considering that 10 mL $L^{-1}$ of water impurities and oxygen impurities still existed in the argon gas, molecular sieves were used to absorb the water impurities, and a sealed canister filled with liquid sodium and heated by a PTC heater was used to absorb the oxygen impurities, ensuring the accuracy of the detection.

Fig. 1(b) demonstrates the structures of the sample chamber and the GP component. The top of the GP component is a circle to facilitate the penetration of the laser beam and the emitted light. In addition, the cylinder at the top was narrowed inward by 1 mm to form a gas duct at the point where the gas inlet was connected to the GP component when it was placed in the sample chamber. Argon gas entering the sample chamber through the gas inlet would move upward through this duct, due to the GP component being spaced a short distance from the top of the sample chamber, and it can effectively form a gas knife to block upwardly dispersing sodium aerosols formed by high-temperature liquid sodium or block sodium splattering caused by the kinetic energy of the laser beam by a transverse force. The bottom of the GP component is a semicircle and a semi-ellipse to minimize the bottom area in case the laser beam and the emitted light can pass through completely. The gas flow moved downward along the inner opening of the GP, creating a downward pressure that changes the direction of the diffusion of the sodium aerosol or sodium splash, causing it to be deposited on the inner sidewall of the GP. The bottom structure and the top duct of the GP form two protective mechanisms that effectively prevent sodium aerosol or liquid sodium splashing from reaching the optics, thereby improving the accuracy and sensitivity of detection.

### 2.2 Sample preparation

Liquid sodium samples doped with different concentrations of Fe and O impurities (China Institute of Atomic Energy, China) were prepared. Information on the samples is listed in Tables S1 and S2 in the SI. The concentration of the Fe impurity for each sample was quantitatively analyzed using dissolution and ICP-OES. The high oxygen concentration was determined using the saturated oxygen solubility curve.[19] The detection environment was an argon-filled glove box, and each detection was performed using a 10 g sample at a heating temperature of 220 °C. 40 replicate measurements for the averaging process of each sample were performed.

## 3 Discussion

### 3.1 Spectra analysis

The Fe and O impurities in the liquid sodium were examined to verify the feasibility of GP-LIBS. As shown in Fig. 2, a typical local spectrum of liquid sodium was observed, and the spectrum is demonstrated in Fig. S1 in the SI. As shown in Fig. 2(a)–(e), it can be found that the emission lines of the elements in liquid sodium were all concentrated below 400 nm, which is surprising as the sodium contained the elements Si, Mg and Ca, such as Mg(II) (279.54 nm), Si(I) (251.60 nm) and Ca(II) (393.35 nm). The emission lines of Fe can be observed at 243.03 nm and 259.94 nm, and the signal intensity at 259.94 nm was chosen as the analysis signal, which is significantly higher than that at 243.03 nm. At 247.84 nm, there was a distinct emission signal where the characteristic peaks of both Fe and C were present. The detection was carried out in an argon gas environment with some C present in the gas, and according to the National Institute of Standards and Technology (NIST), the signal intensity of Fe at 259.94 nm is significantly higher than that at 247.84 nm, so the emission line was identified as the characteristic peak of C. At 600 nm to 840 nm, most of the emission signals are characteristic peaks of Ar. In addition, the characteristic peaks of O were observed at 777.14 nm and 777.90 nm despite the argon environment.

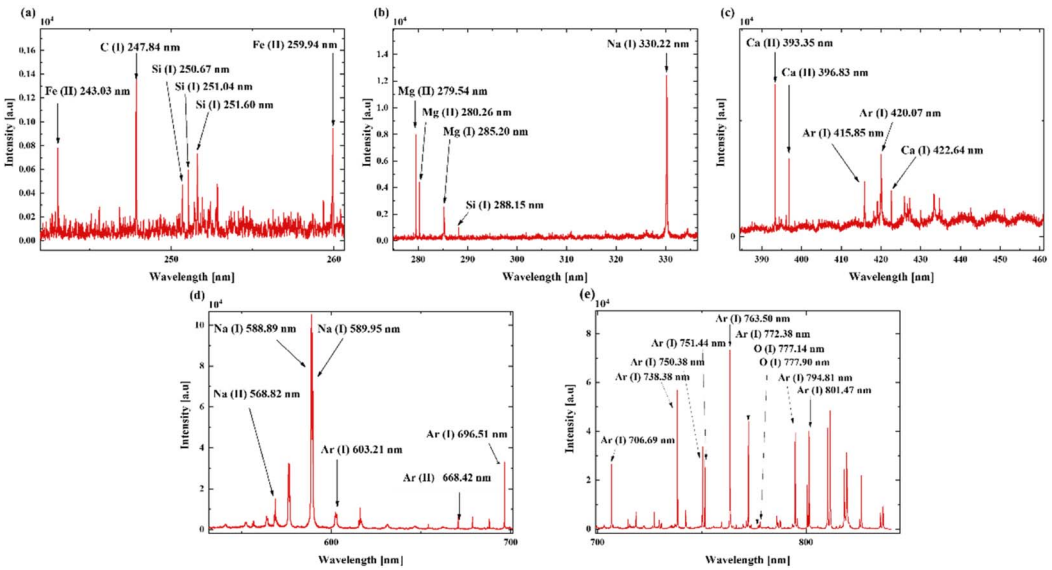


Fig. 2 Typical local spectra of the liquid sodium. (a) Partial spectrum of 230–260 nm. (b) Partial spectrum of 280–330 nm. (c) Partial spectrum of 390–460 nm. (d) Partial spectrum of 550–700 nm. (e) Partial spectrum of 700–810 nm.

### 3.2 Flow rate for the gas-protected component

The sodium aerosols were generated from high-temperature sodium and adhered to the optical lens, which prevented the laser energy from fully reaching the sample, resulting in reduced detection sensitivity. At the same time, contamination of the optical lens occurred because of the splashing of the sodium when the kinetic energy of the pulsed laser was applied to the surface of the liquid sodium. In addition, oxide impurities may be present on the surface of the sodium, which prevent the laser energy from being fully applied to the sample. Therefore, to ensure the accuracy and sensitivity of the detection, a GP component was designed to avoid the above situations and to ensure the detection sensitivity. The design of the GP component enables a high-velocity counterflow gas stream that prevents sodium aerosols from contaminating the lens, and spattered sample was decelerated or deflected (by the gas flow) to avoid direct impact on the lens surface. Hence, the main parameters of the GP structure are the gas flow rate and the stability. Thus, the characteristic peaks of Fe(II) (259.94 nm) and Na(II) (588.95 nm) were selected as the analytical signals to optimize these parameters.

The variation of the signal intensity and background value with gas flow rate is demonstrated in Fig. 3(a). The signal intensity and background value exhibited the same trends with the gas flow rate. When the gas flow rate was lower than 0.4 L $min^{-1}$, the signal intensity and background value were weak. This is because aerosols may penetrate the gas curtain and attach to the lens when the kinetic energy of the gas stream is insufficient, because of the low gas flow rate to effectively deflect upward particles (especially high momentum particles).

Consequently, this led to a decrease in the signal intensity of the Fe impurity. When the gas flow rate was higher than 0.4 L $min^{-1}$, the signal intensity and background value showed a gradual decrease. This is because when the gas flow rate increased, the refractive index of the optical path was not homogeneous due to the changes in the density of the gas flow, which interfered with the accuracy of the laser measurement, thus leading to a decrease in signal intensity. In addition, the faster velocity gas flow rate would blow the liquid sodium, making the surface of the liquid sodium deform, which caused the laser focus to be offset in the longitudinal direction. This resulted in only a portion of the laser energy being applied to the sample, reducing both the signal intensity and the background intensity. As shown in Fig. 3(a), the signal intensity reached a maximum when the gas flow rate was 0.4 L $min^{-1}$. Although the background value was increased at this flow rate, affecting the quantitative analysis, the sensitivity was most important for the detection of impurities in the liquid sodium.

Meanwhile, the laser may act on the oxide on the surface of the liquid sodium. Simultaneously, the optimal flow rate was evaluated based on signal stabilities of Fe(II) (259.94 nm) and Na(II) (588.95 nm), with results shown in Fig. 3(b) and (c). The signal stabilities remained remarkably consistent across different flow rates, and the RSDs were all below 8%. It can be seen that the signal variations were not significant at different flow rates. This is because, despite varying gas flow rates, the plasma region remains consistently saturated with the effect of the GP component. Different gas flow rates only affect the signal intensity. In summary, 0.4 L $min^{-1}$ was selected as the optimal gas flow rate.

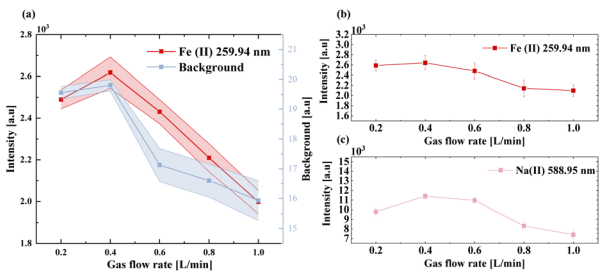


Fig. 3 The optimized results for the gas flow rate of the GP. (a) Variation of signal intensity and background value with the gas flow rate of the GP component. (b) Signal stability of Fe(II) (259.94 nm) with different gas flow rates. (c) Signal stability of Na(II) (588.95 nm) with different gas flow rates.

### 3.3 Parameter optimization of GP-LIBS

The parameters of the laser and spectrometer were optimized to ensure the performance of the GP-LIBS, and the signal of Fe(II) (259.94 nm) was utilized in this section. One of the most important factors of the LIBS system affecting the detection sensitivity is the exposure time of the spectrometer. As demonstrated in Fig. 4(a), the signal-to-background ratio (SBR) increased with the exposure time, while the rate of SBR increase gradually decreased. At the same time, it can be seen that the rate of increase of the signal intensity increased with an increase in exposure time. When the exposure time exceeds 1000 ms, the SBR value changes slowly while the signal strength continues to increase. This means that when the exposure time is too long, the background value increases faster than the signal intensity. Therefore, the exposure time was chosen to be 1000 ms.

The noise could be suppressed by adjusting the number of averaging times, which can reduce the limit of detection (LOD). The signal-to-noise ratio (SNR) as a function of the number of averaging times of the spectrometer is illustrated in Fig. 4(b), and the SNR was decreased when the number of averaging times was more than 10. This indicated that the random noise in this system was mainly suppressed by the spectrometer when the number of averaging times was lower than 10. As the number of averaging times increased, there was a noticeable decrease in the signal intensity of Fe(II) (259.94 nm). This may be attributed to the increased sampling number resulting from the number of averaging times, which caused deformation of the liquid sodium due to the number of the laser irradiations. As a consequence, some invalid spectra were captured because of the focal point shifts, which reduced the signal intensity by averaging, thus reducing the SNR. As indicated in Fig. S2, it can be observed that the SNR exhibits a gradual upward trend after removing invalid spectra, while the signal intensity continues to decrease. Considering that increasing the number of averaging times requires higher sampling numbers and longer sampling

 

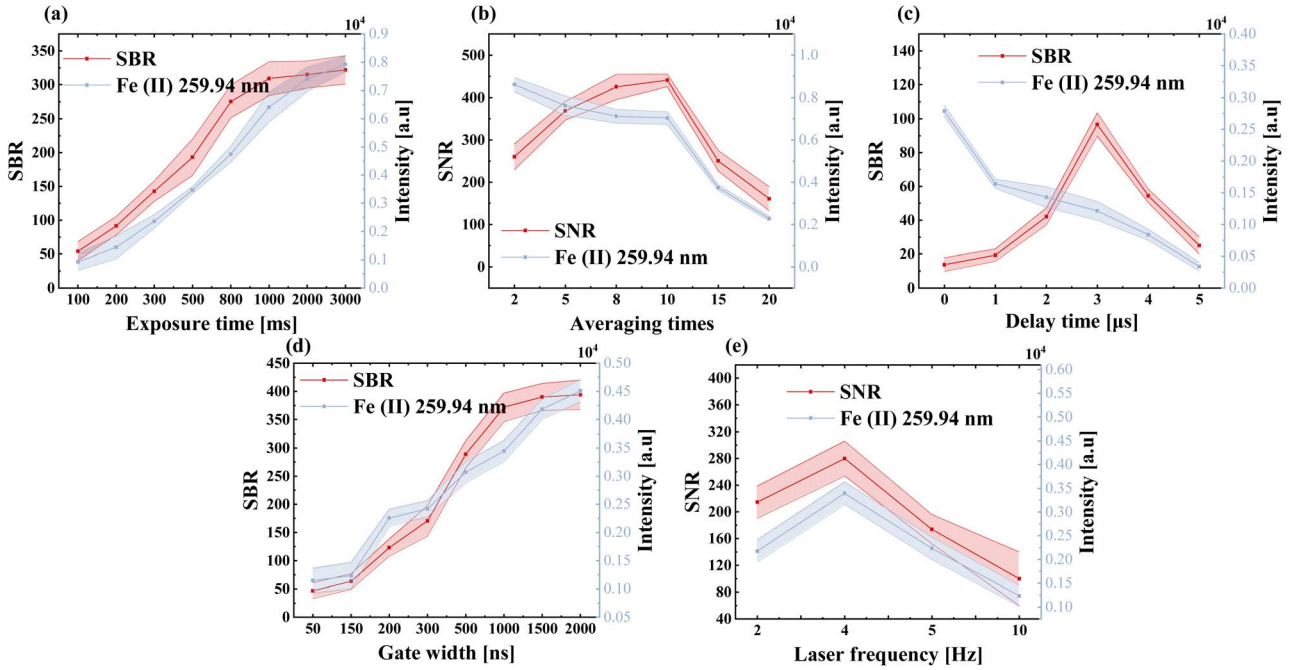


Fig. 4 Optimization results for parameters of LIBS systems. (a) Optimization results for the exposure time of the spectrometer. (b) Optimization results for the number of averaging times of the spectrometer. (c) Optimization results for the delay time of the spectrometer. (d) Optimization results for the gate width of the spectrometer. (e) Optimization results for the frequency of the laser.

times, and that the SNR growth rate slows significantly above 10 averaging times despite removing invalid spectra, the number of averaging times was set to 10 for the subsequent experiment.

The would be generated by the laser-induced plasma in the early stage, which affected the background signal and thus the accuracy of the detection. The bremsstrahlung was mainly suppressed by the delay time, so the SBR was used as the evaluation index of this parameter. At shorter delay times, the higher intensity was mainly due to the presence of the background spectrum. While the signal intensity decreased with increasing delay times, the SBR increased and then decreased. This implied that when the delay times were large, not only was the background spectrum eliminated, but also a part of the signal value was filtered out. Consequently, the delay time was set to 3 μs.

The signal enhancement of the ICCD in the spectrometer was controlled by the gate width. As the gate width increased, both the SBR and signal intensity increased. Similar to the exposure time, as the gate width exceeds 1000 ns, changes in the SBR value become gradual while the signal intensity continues to increase. A gate width of 1000 ns was used for the subsequent analysis.

The laser frequency also impacted the signal emission intensity. As demonstrated in Fig. 4(e), when the laser frequency was low, a lower signal intensity resulted, leading to a reduction in the SNR values. This indicated that the signal intensity obtained at that frequency is not reliable. As the laser frequency increased, the thermal effect of the laser on the sample surface enhanced the signal intensity to some extent, thereby increasing the value of the SNR. When the laser frequency was higher than 4 Hz, the kinetic energy of the laser acting on the surface of the liquid sodium was too large, resulting in the GP component being unable to prevent the liquid sodium from splashing, thus contaminating the optical lens. In addition, with a higher laser frequency, a deformation of the sodium liquid surface occurred, and before the deformation could be reversed, the laser acted again on the sample surface, thus reducing the signal intensity. Therefore, the laser frequency was set to 4 Hz.

### 3.4 Effectiveness of the gas-protected component

To verify the potential impact of GP on the optical transmission efficiency, 40 measurements were taken on identical samples both with and without the GP component, and the results were averaged and are shown in Fig. 5(a). The measured signal exhibits high consistency under both GP and non-GP conditions, thus demonstrating that GP had no impact on the collection efficiency.

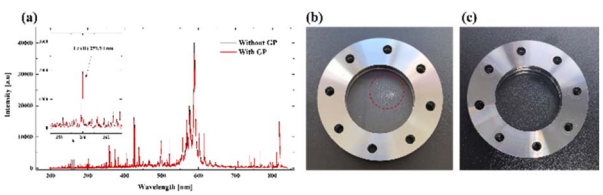


Fig. 5 Effectiveness results of the GP component. (a) Spectra of the same sample with and without the GP component. (b) Flange viewing window without the GP component. (c) Flange window with the GP component.

Additionally, to verify that GP effectively reduces lens contamination, measurements were conducted for 10 min on the same sample under both non-GP and GP conditions. The results are shown in Fig. 5(b) and (c). It can be observed that there were distinct white spots that appeared on the flange viewing window without the GP component. These spots result from liquid sodium splattering caused by laser interaction. In contrast, when the GP was present, no significant contamination was visible on the flange viewing window. Therefore, the GP component not only does not interfere with the transmission of emitted and collected light but also effectively blocks contamination caused by liquid sodium splatter.

### 3.5 Calibration curve and limit of detection

The signal acquisition for different concentrations of Fe was measured under the optimal parameters. In this work, the LOD of Fe was estimated according to the following equation as defined by the International Union of Pure and Applied Chemistry (IUPAC): $\mathrm{LOD} = \frac{3\sigma}{k}$, where $\sigma$ denotes the spectral noise (standard deviation of the background) and $k$ is the slope of the calibration curve. The results of the calibration curve of Fe and the signal intensity are shown in Fig. 6. It is worth mentioning that the LOD of the Fe impurity in liquid sodium was calculated to be 0.68 mg $L^{-1}$, and all the RSDs of the signal intensity were lower than 7%.

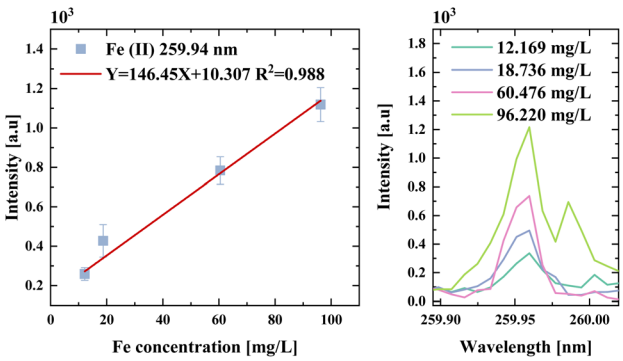


Fig. 6 Calibration curve for Fe(ii) (left) and the corresponding spectra showing signal intensity at various concentrations (right).

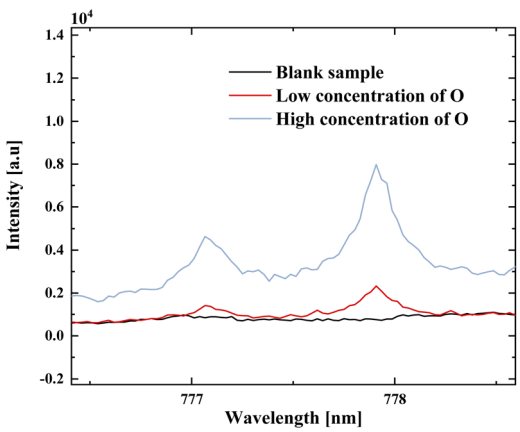


Fig. 7 The emission peaks of blank liquid sodium, and high and low concentrations of the O impurity in liquid sodium.

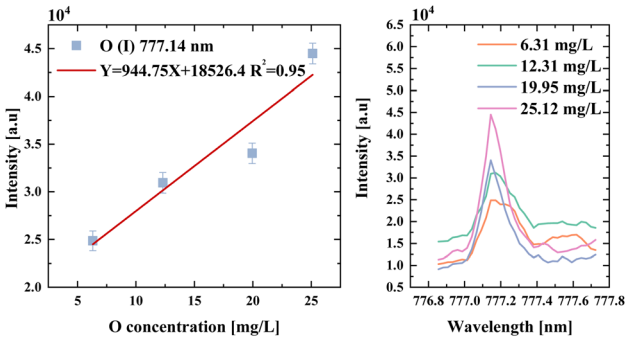


Fig. 8 Calibration curve for O(i) (left) and the corresponding spectra showing signal intensity at various concentrations (right).

To exclude interference from the presence of oxygen in the detection environment, a blank sample, and samples with high and relatively low concentrations of O were analyzed. As demonstrated in Fig. 7, the emission peak for O(I) (777.14 nm) was absent for the blank sample. For liquid sodium samples with high and low concentrations of O impurities, there was a significant difference in the signal intensity for O(I) (777.14 nm) and the signal intensity showed the same trend as the concentration. Furthermore, the calibration curve for O and the signal intensity are shown in Fig. 8. It is worth noting that the LOD of the O impurity in liquid sodium was calculated to be 0.11 mg $L^{-1}$, and all the RSDs of the signal intensity were lower than 4%. The results indicated that the GP-LIBS realized sensitive, stable, real-time monitoring of O and Fe impurities in liquid sodium.

## 4. Conclusions

In this work, a GP-LIBS device was developed for Fe and O impurity detection in liquid sodium in nuclear power plants. A GP component was designed to prevent the upward diffusion of sodium aerosols generated by high-temperature liquid sodium from contaminating the optical lens. Meanwhile, the GP component can also avoid the splashing of liquid sodium due to the kinetic energy of the laser acting on the sample surface. In addition, the GP structure can effectively disperse the oxide impurities on the surface of the liquid sodium, so that the laser can be completely applied to the sample, which ensures the accuracy of the detection. Furthermore, GP-LIBS was able to quantitatively analyze the Fe and O impurities in liquid sodium with LODs of 0.68 mg $L^{-1}$ and 0.11 mg $L^{-1}$, and RSDs of less than 7% and 4%, respectively. The results showed that GP-LIBS can realize sensitive, stable, and real-time monitoring of trace impurity elements in sodium coolant. Consequently, GP-LIBS is expected to become an online monitoring device for sodium coolant in sodium-cooled fast reactor circuits, providing a safety guarantee for the operation of nuclear power plants.

## Conflicts of interest

There are no conflicts to declare.

## Data availability

The data supporting this article have been included as part of the supplementary information (SI). Supplementary information: Table S1 (sample information), Fig. S1 (a typical spectrum of the liquid sodium), and Fig. S2 (the results of average times calculated with invalid spectra removed). See DOI: https://doi.org/10.1039/d5ja00438a.

## Acknowledgements

This work was supported by the State Administration of Science, Technology and Industry for National Defense (grant no. HNKF202305).

## References

1 T. Sofu, *Nucl. Eng. Technol.*, 2015, **47**, 227–239.
2 D. Martelli, A. Del Nevo, M. Angiolini, A. Pietro, M. Tarantino, G. Grasso, F. Lodi, R. Marinari, M. Utili, C. Sartorio, I. di Piazza, D. Diamanti, S. Bassini, S. Cataldo, P. Lorusso, C. Ciantelli and C. Cristalli, *Arabian J. Sci. Eng.*, 2025, **50**, 3293–3301.
3 Y. P. Shapovalov and A. P. Brovko, *Ind. Lab.*, 1980, **46**, 352–355.
4 S. Hémery, T. Auger, J. L. Courouau and F. Balbaud-Célérier, *Corros. Sci.*, 2013, **76**, 441–452.
5 P. Skeldon, J. P. Hilditch, J. R. Hurley and D. R. Tice, *Corros. Sci.*, 1994, **36**, 593.
6 J. S. B. Rao, R. Senthilvadivu, G. Kumar, A. Suriyanarayanan, K. Sundararajan and R. Kumar, *Prog. Nucl. Energy*, 2022, **152**, 104394.
7 S. S. Ximeng Wen, S. Hong and S. Ji, *Anal. Chem.*, 1982, 347–350.
8 R. Ganesan, V. Jayaraman, S. R. Babu, R. Sridharan and T. Gnanasekaran, *J. Nucl. Sci. Technol.*, 2011, **48**, 483–489.
9 X. W. SunZhang Hong, *At. Energy Sci. Technol.*, 1984, 307–311.
10 C. Xie, *Chin. J. Nucl. Sci. Eng.*, 2008, 224–227+248.
11 L. W. Zeng, W. H. Kong, S. Chen, Y. Rao, M. F. Wu, Y. X. Duan, Q. W. Fan, X. Wang and Z. W. Luo, *IEEE Trans. Instrum. Meas.*, 2023, **72**, 1–8.
12 Y. Rao, L. W. Zeng, M. F. Wu, W. H. Kong, W. X. Ren, S. Chen, Q. W. Fan, Y. X. Duan, X. Wang and J. Wang, *J. Anal. At. Spectrom.*, 2023, **38**, 693–703.
13 L. X. Han, C. H. Ma, Z. X. Gao and X. Z. Tang, *Proceedings of International Conference on Photonics and Optical Engineering (icPOE)*, Xi'an, People's Republic of China, 2015.
14 M. Burger, L. A. Finney, L. Garrett, S. S. Harilal, K. C. Hartig, J. Nees, P. J. Skrodzki, X. Xiao and I. Jovanovic, *Spectrochim. Acta, Part B*, 2021, **179**, 106095.
15 A. V. Skalny, T. Korobeinikova, M. Aschner, O. Baranova, E. G. Barbounis, A. Tsatsakis and A. A. Tinkov, *J. Trace Elem. Med. Biol.*, 2023, **79**, 127241.
16 G. S. Senesi, *Earth-Sci. Rev.*, 2014, **139**, 231–267.
17 S. Nisar, A. Alsalme, R. Zulfiqar, M. Rizwan, D. K. Kim, G. Dastgeer and Z. M. Shazad, *Mod. Phys. Lett. B*, 2024, **38**, 2450124.
18 C. Maury, J. B. Sirven, M. Tabarant, D. L'Hermite, J. L. Courouau, C. Gallou, N. Caron, G. Moutiers and V. Cabuil, *Spectrochim. Acta, Part B*, 2013, **82**, 28–35.
19 M. R. Hobdell and C. A. Smith, *J. Nucl. Mater.*, 1982, **110**, 125–139.